JOURNAL OF COMPUTATIONAL PHYSICS 120, 157–170 (1995)

Simultaneous Viscous–Inviscid Coupling via Transpiration

K. F. C. YIU AND M. B. GILES

Oxford University Computing Laboratory, Wolfson Building, Parks Road, Oxford OX1 3QD, United Kingdom

Received December 13, 1993; revised December 24, 1994

In viscous–inviscid coupling analysis, the direct coupling technique and the inverse coupling technique are commonly adopted. However, stability and convergence of the algorithms derived are usually very unsatisfactory. Here, by using the transpiration technique to simulate the effect of the displacement thickness, a new simultaneous coupling method is derived. The integral boundary layer equations and the full potential equation are chosen to be the viscous–inviscid coupled system. After discretization, the Newton–Raphson technique is proposed to solve the coupled nonlinear system. Several numerical results are used to demonstrate the accuracy and efficiency of the proposed method.

1. INTRODUCTION

In viscous flow calculations, viscosity usually plays a significant role in a small region consisting of the boundary layer and the wake, whereas the rest of the flow field is mainly inviscid. This approximation is applicable for many practical cases. One way to explore this characteristic of the flow field is to use the so-called parabolic or thin-layer Navier–Stokes equations, which is intermediate between the full Navier–Stokes equations and the parabolic boundary layer equations. Reduced forms of the Navier–Stokes equations are usually more economical to solve. This technique is most useful when there is a dominant flow direction and the elliptic nature of the flow is not strong. However, when the flow field contains separated regions, it may offer little advantages over the full Navier–Stokes equations. Moreover, at least for the present time, methods using any form of the Navier–Stokes equations have fairly poor transition models and cannot handle transitional separation bubbles.

Another way is to use separate equations for the viscous dominant region and the inviscid region. The governing equation therefore consists of two coupled equations: a viscous equation governs the boundary layer and the wake and an inviscid equation governs the rest of the flow field. In solving the two coupled equations, the traditional ways are the direct coupling approach and the inverse coupling approach, which involve iterating on both equations alternatively until convergence. However, both coupling approaches can be unstable and convergence rates are usually extremely slow [13]. A refinement to the above two approaches is the semi-inverse approach, which improves on the stability of the iterative process. However, when the boundary layer grows thicker or if the flow is separated, severe under-relaxation is required in updating the variables and the resulting convergence rate is inevitably very slow [7]. This clearly indicates the limitation of using the semi-inverse approach.

Various authors have explored the possibility of solving the coupled equations simultaneously. Methods derived includes the quasi-simultaneous coupling approach [12] and the fully simultaneous approach in [10]. In solving the two coupled equations, the location of the boundary between the viscous flow and the inviscid flow must be easy to handle in order to impose the coupling condition and to know where to start inviscid calculations. In [10], the location of this boundary is traced in the physical computational domain; very complicated interpolation formulas and discretization formulas are inevitably involved which is very difficult to implement, especially when the computational domain becomes more irregular and complicated. Therefore, special methods are required which can handle the arbitrariness of the boundary layer thickness.

One method is to use the streamline coordinates system to discretize the inviscid equation [3, 4], which turns out to be very successful. Here, another method, namely the transpiration technique is used. Transpiration is a technique in which extra nonphysical normal flows are created on the blade surface and along a wake line in order to form a new streamline pattern such that the surface streamlines no longer follow the blade surface under inviscid flow. This technique can be used to simulate the boundary layer thickness very efficiently and has been used in [11, 7, 9] in a semi-inverse coupling context. In this paper, the transpiration technique is used to provide a new simultaneous coupling technique. The full potential equation is used to govern the inviscid flow field while the integral boundary layer equations are used to calculate the viscous effect. After discretization, the Newton–Raphson method is used to solve the coupled systems simultaneously. Various test cases are used to illustrate the accuracy of the transpiration technique and the efficiency of using the Newton–Raphson method.

0021-9991/95 $12.00

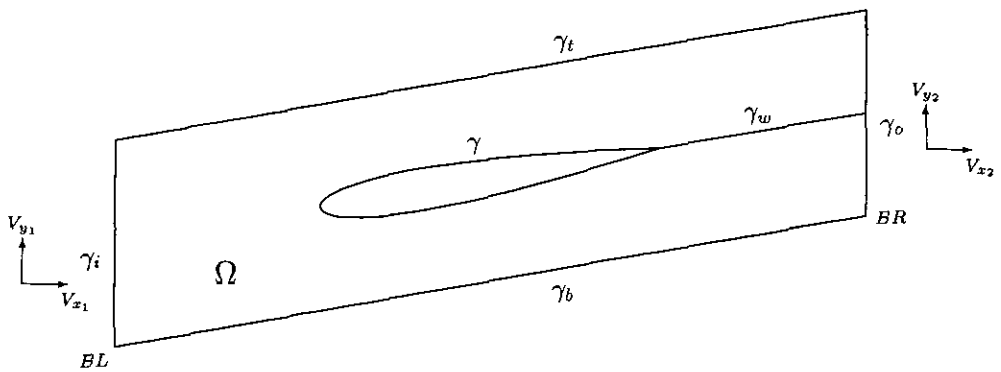

FIG. 1. The computational domain for cascades.

2. FORMULATION

In the following, the problem will be formulated for internal flow calculations. Assuming the flow is isentropic and irrotational, then the velocity potential exists and the continuity equation becomes

$$\nabla \cdot (\rho \nabla \phi) = 0 \tag{2.1}$$

which is known as the full potential equation. In order to calculate the density, the energy equation is used, which can be integrated to give

$$\frac{c^2}{\tilde{\gamma} - 1} + \frac{|\mathbf{u}|^2}{2} = \text{const}, \tag{2.2}$$

where c is the speed of sound and $\tilde{\gamma}$ is the ratio of specific heats. For internal flow, the constant is usually more convenient to be evaluated at the stagnation point and (2.2) becomes

$$\frac{c^2}{\tilde{\gamma}_{-1}} + \frac{|\mathbf{u}|^2}{2} = \frac{c_0^2}{\tilde{\gamma} - 1}, \tag{2.3}$$

where the subscript 0 denotes evaluation at the stagnation point. By using the isentropic relations[1]

$$p = \tilde{\alpha} \rho^{\tilde{\gamma}} \tag{2.4}$$

$$c^2 = \tilde{\gamma} p / \rho, \tag{2.5}$$

where $\tilde{\alpha}$ is a constant, the density is finally given by

$$\frac{\rho}{\rho_0} = \left(1 - \frac{\tilde{\gamma} - 1}{2} \frac{|\mathbf{u}|^2}{c_0^2}\right)^{1/(\tilde{\gamma} - 1)}. \tag{2.6}$$

A sample computational domain is depicted in Fig. 1. A cut γ_w is introduced which joins the trailing edge of the blade with the outer boundary. By the definition of the circulation,

$$\beta = \oint_C \mathbf{u} \cdot d\mathbf{s} = \phi^+ - \phi^- \quad \text{on } \gamma_w, \tag{2.7}$$

where C is any curve in the flow field enclosing the blade. As the circulation β is introduced in order to allow lift to the airfoil, one extra equation is required and is provided by the Kutta condition, which forces the equality of the velocity leaving the trailing edge on the upper and the lower surface. On γ_i and γ_b, the periodic condition is imposed as

$$\phi_{\gamma_i} - \phi_{\gamma_b} = s V_{y1}, \tag{2.8}$$

where s is the spacing between consecutive blades and V_{y1} is the inlet velocity tangential to γ_i. In internal flow, an extra condition is required in order to fix the shock position. A detailed study of the condition is given by Deconinck and Hirsch [2] and more details are discussed in [6]. The condition

$$\phi_{BR} - \phi_{BL} = \text{const} \tag{2.9}$$

is used here, where the subscripts BR and BL are defined in Fig. 1. Following [14], the physical quantities which are chosen as the inputs are the inlet tangential velocity V_{y1}, the stagnation density ρ_0 and the stagnation speed of sound c_0. In practice, ρ is scaled by ρ_0 so that $\rho_0 = 1$, while ϕ is scaled by $u_{\text{nom}} \Delta s \equiv \phi_{BR} - \phi_{BL}$ so that the scaled ϕ has a jump equal to 1 in (2.9). The velocity and the speed of sound are scaled by the nominal velocity u_{nom} so that $u_{\text{nom}} = 1$. Consequently, two variables left as input are

$$\mu_1 = 1/c_0 \tag{2.10}$$

$$\mu_2 = V_{y1}/c_0. \tag{2.11}$$

For transonic calculations, the artificial compressibility [5, 8] is used. Define $\partial\rho/\partial s$ as upwind streamwise derivative; the

[1] See, for example, [1, p. 321].

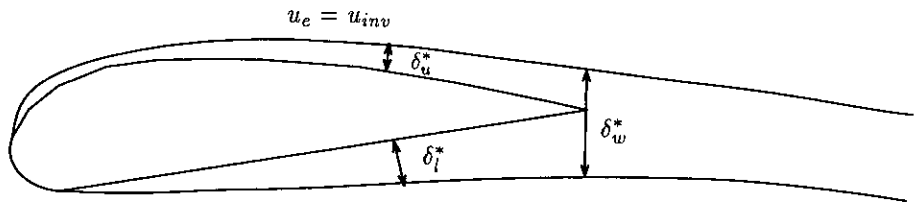

FIG. 2. The coupling conditions.

density is modified as

$$\tilde{\rho} = \rho - \nu \frac{\partial \rho}{\partial s} \Delta s \tag{2.12}$$

in which ν is a switching function chosen as [14]

$$\nu = \begin{cases} \nu_0 M^{2\nu_1/\nu_0} e^{-\lambda(M-1)^2} & \text{if } M < 1 \\ \nu_0 + \nu_1(1 - 1/M^2) & \text{if } M \geq 1 \end{cases} \tag{2.13}$$

where ν_0, ν_1, λ are constants.

In coupling the viscous effect with the inviscid solutions, there are two coupling conditions (Fig. 2). The first condition is the presence of the boundary layer thickness. The surface streamline is moved from the blade surface by the distance equal to the displacement thickness. The second condition is the equality of flow quantities at the edge of the boundary layer. The boundary layer edge velocity used in the boundary layer equations must be equal to the local inviscid velocity calculated by the inviscid solver. In order to simulate the streamline movements induced by the displacement thickness, a surface transpiration technique is employed. From Fig. 3, the simplest transpiration model is used and is given by

$$\rho w_n = \frac{\partial}{\partial s}(\rho w_s \delta^*), \tag{2.14}$$

where $w_s = \partial\phi/\partial s$ is the tangential velocity calculated on the blade surface, $w_n = \partial\phi/\partial n$ is the velocity normal to the blade surface and δ^* is the displacement thickness. Using (2.14) to replace the solid wall boundary condition and the normal flux cancellation along the wake, the weak formulation of the full potential equation gives

$$\int_\Omega \rho \nabla\phi \cdot \nabla N_i \, dx = \int_{\gamma+\gamma_w} \rho w_s \delta^* \frac{dN_i}{ds} ds + \int_{\gamma_i} \rho \frac{\partial \phi}{\partial n} N_i \, ds + \int_{\gamma_0} \rho \frac{\partial \phi}{\partial n} N_i \, ds \quad \forall N_i \in H^1(\Omega), \tag{2.15}$$

where H^1 is a Sobolev space. In order to include the viscous effects, the integral boundary layer equations are used. The boundary layer development is governed by two principal equations, namely the von Karman integral momentum equation and the integral kinetic energy equation. In practice, the kinetic energy is not used directly. Instead it is combined with the momentum equation to give the so-called shape parameter equation.[2] In the laminar region, a disturbance amplification equation is used to determine the transition location. The method is based on the Orr–Sommerfeld equation and is known as the e^9 method. Once transition starts, the flow becomes turbulent and a dissipation lag equation is used instead to model upstream

[2] See [3 or 4].

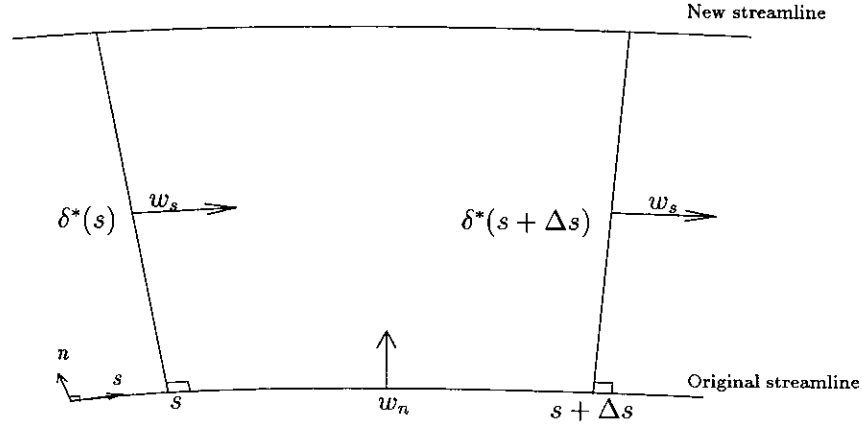

FIG. 3. Control volume.

history effects. In the transition interval, the momentum equation and the shape parameter equation are simply taken to be the weighted averages of their laminar and turbulent counterparts. More details of the integral boundary equations employed here and all the closure relations can be found in [3, 4].

The final coupled system can be summarized as

$$\int_\Omega \rho \nabla \phi \cdot \nabla N_i \, dx = \int_{\gamma+\gamma_w} \rho w_s \, \delta^* \frac{dN_i}{ds} \, ds + \int_{\gamma_i} \rho \frac{\partial \phi}{\partial n} N_i \, ds + \int_{\gamma_0} \rho \frac{\partial \phi}{\partial n} N_i \, ds \quad \forall N_i \in H^1(\Omega) \tag{2.16}$$

$$\frac{d\theta}{ds} = F_1(\theta, \delta^*, u_e) \tag{2.17}$$

$$\frac{dH^*(\theta, \delta^*, u_e)}{ds} = F_2(\theta, \delta^*, u_e, C_\tau) \tag{2.18}$$

$$\frac{dC_\tau}{ds} = F_3(\theta, \delta^*, u_e, C_\tau) \quad \text{in turbulent region} \tag{2.19}$$

$$\frac{d\tilde{n}}{ds} = F_4(\theta, \delta^*, u_e) \quad \text{in laminar region} \tag{2.20}$$

$$u_e - w_s = 0 \tag{2.21}$$

$$|(w_s)_{te_u}| = |(w_s)_{te_l}|, \tag{2.22}$$

where (2.17) denotes the integral momentum equation, (2.18) denotes the shape parameter equation, (2.19) denotes the dissipation lag equation, (2.20) denotes the disturbance amplification equation, (2.21) is the velocity coupling condition, and (2.22) is the Kutta condition in which the subscripts te_u and te_l are defined in Fig. 5. In the formulation, the equality of the edge velocity and the inviscid velocity is treated as an equation rather than using w_s directly in the integral boundary layer equations. This is because if w_s is used directly, the formulation resembles using a direct coupling technique to solve the integral boundary layer equations which may not converge for separated flows.

3. DISCRETIZATION AND SOLUTION

In discretizing the full potential equation (2.16), the finite element method is used. Let $\mathcal{T}_h = \{T_k\}$ be a family of triangles parametrized by h, the maximum edge length over all the triangles. Because of the imposed boundary conditions described in the last section, the potential ϕ is determined uniquely up to an arbitrary constant. This problem can be solved by simply fixing the value of ϕ at one point within the computational domain and the following is chosen:

$$\phi_{BL} = 0. \tag{3.1}$$

Thus, after scaling, (2.9) gives

$$\phi_{BR} = 1. \tag{3.2}$$

Define the conforming piecewise linear function space as

$$H_h^1 = \{v_h \in C^0(\bar{\Omega}) : v_h|_T \in P^1(T) \; \forall T \in \mathcal{T}_h\}, \tag{3.3}$$

where $P^1(T)$ is the space of polynomials of degree 1 on T and $C^0(\bar{\Omega})$ is the space of continuous function on $\bar{\Omega}$. Together with the jump condition (2.7) for the circulation and (2.8) for the periodic condition, we introduce the finite dimensional space

$$V_{h,\Gamma}^{\alpha,\eta} = \{v \in H_h^1 : v^+ - v^- = \alpha \text{ on } \Sigma, v_{\gamma_i} - v_{\gamma_b} = \eta, \; v_{BL} = 0, v_{BR} = 1\}. \tag{3.4}$$

Thus, ϕ is in the space $V_{h,\Gamma}^{\beta,\eta}$, where β is the amount of circulation and $\eta = sV_{y1}$ which is defined in (2.8). The test space is chosen to be the space

$$V_h^{0,0} = \{v \in H_h^1 : v^+ - v^- = 0 \text{ on } \Sigma, v_{\gamma_i} - v_{\gamma_b} = 0, \; v_{BL} = 0, v_{BR} = 0\}. \tag{3.5}$$

At the inlet and outlet, the average velocities are calculated as

$$(\bar{V}_{x_1}, \bar{V}_{y_1})^T = \frac{1}{n_{\text{in}}} \sum_{e=1}^{n_{\text{in}}} (\nabla \phi)_e^T \tag{3.6}$$

$$(\bar{V}_{x_2}, \bar{V}_{y_2})^T = \frac{1}{n_{\text{out}}} \sum_{e=1}^{n_{\text{out}}} (\nabla \phi)_e^T \tag{3.7}$$

where n_{in} and n_{out} denote the number of inlet and outlet elements, respectively; typical inlet and outlet elements applied in the summations are depicted in Fig. 4. The average velocities calculated by (3.6) and (3.7) are used to approximate the inlet and outlet boundary conditions as

$$\rho \frac{\partial \phi}{\partial n} = -\rho(\bar{V}_{x_1}, V_{y_1}) \bar{V}_{x_1} \quad \text{on } \gamma_i \tag{3.8}$$

$$\rho \frac{\partial \phi}{\partial n} = \rho(\bar{V}_{x_2}, \bar{V}_{y_2}) \bar{V}_{x_2} \quad \text{on } \gamma_0, \tag{3.9}$$

where the inlet tangential velocity V_{y_1} imposed in (2.8) is used in (3.8). Following the discussion above, the full potential equa-

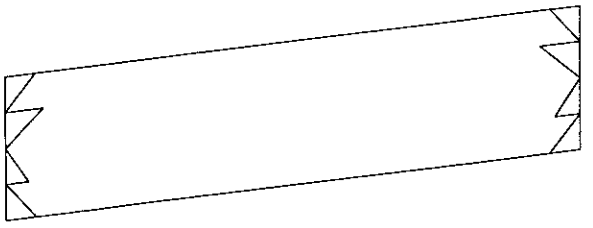

FIG. 4. The inlet and outlet elements.

tion (2.16) is finally discretized as

$$\int_\Omega \tilde{\rho}\nabla\phi\cdot\nabla N_i\,dx = \int_{\gamma+\gamma_w} \rho w_s\,\delta^*\frac{dN_i}{ds}\,ds - \int_{\gamma_i}\rho\bar{V}_{x_1}N_i\,ds + \int_{\gamma_0}\rho\bar{V}_{x_2}N_i\,ds \quad \forall N_i\in V_h^{0,0}. \tag{3.10}$$

In discretizing (2.22), a second-order one-sided finite difference approximation is used. The final discretization of (2.22) can be denoted by

$$F(\phi) = 0. \tag{3.11}$$

In discretizing the integral boundary layer equations, the same grid points on the blade surface for the finite element discretization are used. The blade is divided into upper and lower surfaces by the stagnation point and the trailing edge (Fig. 5). Starting from the stagnation point, the accumulated arc length s for each surface is calculated and is continued into the wake (Fig. 6). The equations are discretized using s along the flow direction. The momentum equation (2.17) and the shape parameter equation (2.18) are discretized using the logarithmic central differences. In turbulent region, the shear stress coefficient lag equation (2.20) is discretized by the backward Euler method; while in laminar region, the amplification equation (2.20) is discretized by the forward Euler method. More details about the discretization can be found in [3]. At the first grid point after the stagnation point, the boundary layer is assumed to be similar and the derivative terms there are set to their known values obtained from the similarity boundary layer theory.

Along the wake, all the boundary layer varibles are defined as single variables instead of dividing into upper and lower surface variables (Fig. 5); and the accumulated arc length of the wake is calculated after the trailing edge of the lower surface (Fig. 6). Therefore, special joining conditions are required at the trailing edge to initialize the wake calculations. In particular, the variables

$$\delta^*_{w_0} = \delta^*_{te_l} + \delta^*_{te_u} \tag{3.12}$$

$$\theta_{w_0} = \theta_{te_l} + \theta_{te_u} \tag{3.13}$$

$$(C_\tau)_{w_0} = \frac{(C_\tau)_{te_l}\theta_{te_l} + (C_\tau)_{te_u}\theta_{te_u}}{\theta_{te_l} + \theta_{te_u}} \tag{3.14}$$

are chosen to be the initial wake variables in discretizing the equations in the interval $[s_{te_l}, s_{w_1}]$.

In the discretization, the boundary layer edge velocity u_e is defined at the node while the inviscid velocity w_s is defined at the mid-node (Fig. 6). One simple way to discretize (2.21) is to use averaging for w_s so that

$$u_{e_i} - \tfrac{1}{2}(w_{s_{i-1/2}} + w_{s_{i+1/2}}) = 0. \tag{3.15}$$

However, averagings are prone to the sawtooth spurious mode, which can easily be triggered off at the separation point or at the trailing edge region. Therefore, whenever the solutions appear to have sawtooth spurious modes, the following upwind approximation

$$u_{e_i} - w_{s_{i-1/2}} = 0 \tag{3.16}$$

is used instead. Combining the formulas (3.15) and (3.16), we have

$$u_{e_i} - (\tfrac{1}{2}(1 + i_{up})w_{s_{i-1/2}} + \tfrac{1}{2}(1 - i_{up})w_{s_{i+1/2}}) = 0, \tag{3.17}$$

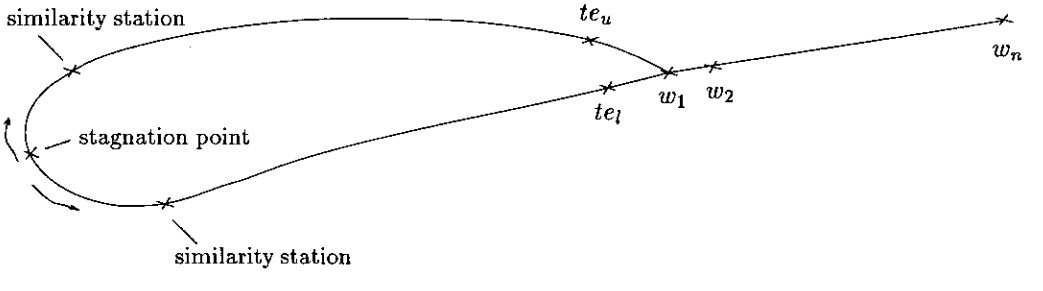

FIG. 5. The boundary layer grid stations.

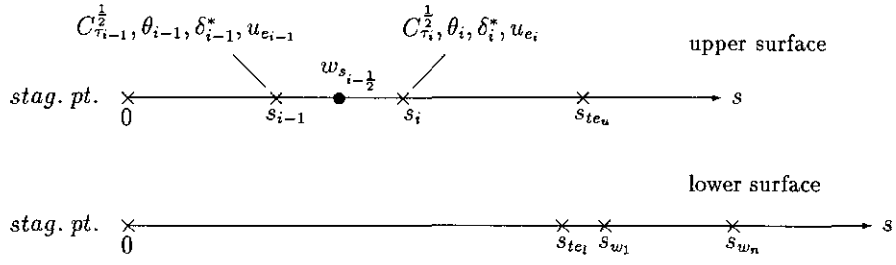

FIG. 6. The accumulated arc length coordinates.

where

$$i_{up} = \begin{cases} 0 & \text{if the averaging formula is used,} \\ 1 & \text{if the upwind formula is used.} \end{cases}$$

In solving the system of discretized nonlinear equations, the Newton–Raphson technique is used. In the kth iteration, the Jacobian matrix is assembled and it reduces to solving the system of linear equations

$$B^{(k)}(\delta\phi, N_i) - B^{(k)}_{\gamma+\gamma_w}(\delta\phi, N_i) = -R^{(k)}_{\phi_i} \quad \forall N_i \in V_h^0 \tag{3.18}$$

$$A^{(k)}_{i-1}\,\delta\boldsymbol{\tau}_{i-1} + A^{(k)}_i\,\delta\boldsymbol{\tau}_i = -R_{v_{i+1/2}} \quad \forall s_i \in [s_{1_u}, s_{te_u}] \cup [s_{1_l}, s_{w_n}] \tag{3.19}$$

$$\delta u_{e_i} - (\tfrac{1}{2}(1 + i_{up})\,\delta w_{s_{i-1/2}} + \tfrac{1}{2}(1 - i_{up})\,\delta w_{s_{i+1/2}})) = 0$$

$$\forall s_i \in [s_{1_u}, s_{te_u}] \cup [s_{1_l}, s_{w_n}] \tag{3.20}$$

$$F^{(k)}(\delta\phi) = -F^{(k)}(\phi) \tag{3.21}$$

for $\delta\phi$ and $\delta\tau$, where B denotes the linearization of the domain integral and $B_{\gamma+\gamma_w}$ denotes the linearization of the surface integral on γ and γ_w in (3.10); $A \in \mathbb{R}^{3\times4}$ denotes the linearization of the integral boundary layer equations and $\boldsymbol{\tau}^T = (C_\tau^{1/2}, \theta, \delta^*, u_e)^T$ or $(\tilde{n}, \theta, \delta^*, u_e)^T$. In solving the system of linear equations, (3.20) is not directly used. Instead it is substituted into (3.19) to eliminate u_e. In order to solve the system efficiently, the band structure of (3.18) should be maintained as far as possible. Therefore, in assembling the Jacobian matrix, the order of the equations should be well arranged. Recall that in finite element discretizations, each node is assigned a node number and each node number corresponds to one equation and one variable. Thus, in accommodating the linearized boundary layer equations (3.19) into the Jacobian matrix, each blade surface node and each node along the wake is counted four times and the linearized boundary layer equations are put immediately after the nodal equation. The banded system is simply solved by LU decomposition.

The final algorithm can be summarized as:

(0) Solve the inviscid problem.

(1) Calculate the stagnation point.

(2) Initialize the boundary layer variables.

(3) Evaluate the Jacobian matrix.

(4) Solve the system of linearized equations.

(5) Update the variables.

(6) Recalculate the stagnation point.

(7) Solve the integral boundary equations using a hybrid coupling marching technique.

(8) Return to step 3 until convergence.

In the initialization stage of the boundary layer variables in step 2, the integral boundary layer equations are solved station after station by marching along the flow direction starting from the stagnation point (Fig. 6). When the kinematic shape parameter H_k defined by

$$H_k = \frac{\delta^*/\theta - 0.290M_e^2}{1 + 0.113M_e^2} \tag{3.22}$$

is not too large, a direct coupling step is executed at that station by fixing the edge velocity to be the inviscid velocity using (3.17). When H_k is larger than a predefined threshold value, an inverse coupling step is used instead, where H_k is fixed to be the extrapolated value from the downstream solutions. In updating the variables in step 5, the relaxation factor is chosen such that the boundary layer variables are not allowed to change more than a certain predefined percentage. In step 7, the integral boundary layer equations are solved by using a special hybrid coupling marching technique, which is used in the program MISES [3, 15]. Denote $\overline{H}_k$ and $\overline{u}_e$ as the updated variables using the Newton–Raphson technique in step 5. The hybrid coupling marching technique is to solve the integral boundary layer equations (2.17), (2.18), (2.19), or (2.20), together with the equation

$$\overline{H}_k^2\left(\frac{H_k}{\overline{H}_k} - 1\right) + \omega\frac{du_e}{dH_k}\left(\frac{u_e}{\overline{u}_e} - 1\right) = 0, \tag{3.23}$$

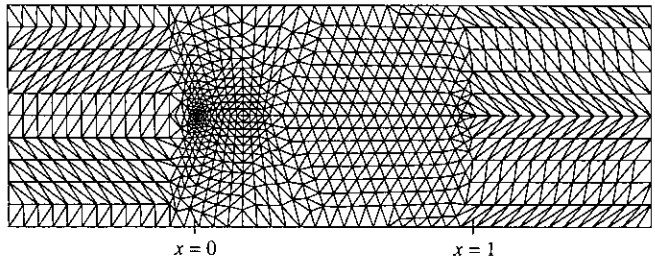

FIG. 7. The mesh for test case 1.

where ω is a large constant. Like step 2, the solutions are calculated station after station by marching from the stagnation point along the flow direction. The reason for having step 7 in the algorithm is mainly to accelerate the convergence of the algorithm, especially when the flow is separated. Although the simultaneous coupling technique converges rapidly for most of the cases, its performance is still not very satisfactory in calculating separated flow. By including the hybrid coupled marching which fixes the location of separation more accurately and efficiently, the overall performance becomes much better.

4. NUMERICAL RESULTS

The main aims of the test cases presented here is to demonstrate the accuracy and the efficiency of the boundary layer coupling procedure using the transpiration technique. Three test cases will be presented. The number of iterations quoted below is the first iteration to drive

$$\max(\|\delta\phi\|_\infty, \|\delta\tau\|_\infty) < 0.005, \tag{4.1}$$

where $\delta\tau$ is defined in (3.19). The program FINSUP, developed initially in [14] and has been used in Rolls Royce plc, is employed for solving the full potential equation.

Since the program MISES described in [3–15] has been verified rigorously with experimental results and is presently being used in several aerospace companies, the first test problem is designed to make a comparison of results between present method and MISES. The flat plate is used with zero stagger. The mesh is displayed in Fig. 7, where the flat plate is located in the centre of the mesh together with refinements at the leading edge. The x coordinate of the leading edge and the trailing edge is 0 and 1, respectively. The Reynolds number is 0.5×10^4 and the inlet Mach number is 0.11. The averaging formula (3.15) is used in calculating the edge velocity. The algorithm converges in two iterations. The resulting displacement and the momentum thickness is compared in Fig. 8 and the velocity distribution converges in Fig. 8 and the velocity distribution is compared in Fig. 9. A good agreement is achieved which demonstrates that the present transpiration model gives fairly good results. Note that after the trailing edge, the total displacement thickness and the total momentum thickness are plotted.

The second test case deals with a low speed compressor used in [15]. The mesh is depicted in Fig. 10. The Reynolds number is 0.478×10^6, the inlet Mach number is 0.12 and the inlet and the outlet angle of attack is 37° and 1.2°, respectively. The upwind formula (3.16) is used on and before the separation point while the average formula (3.15) is used for the rest of

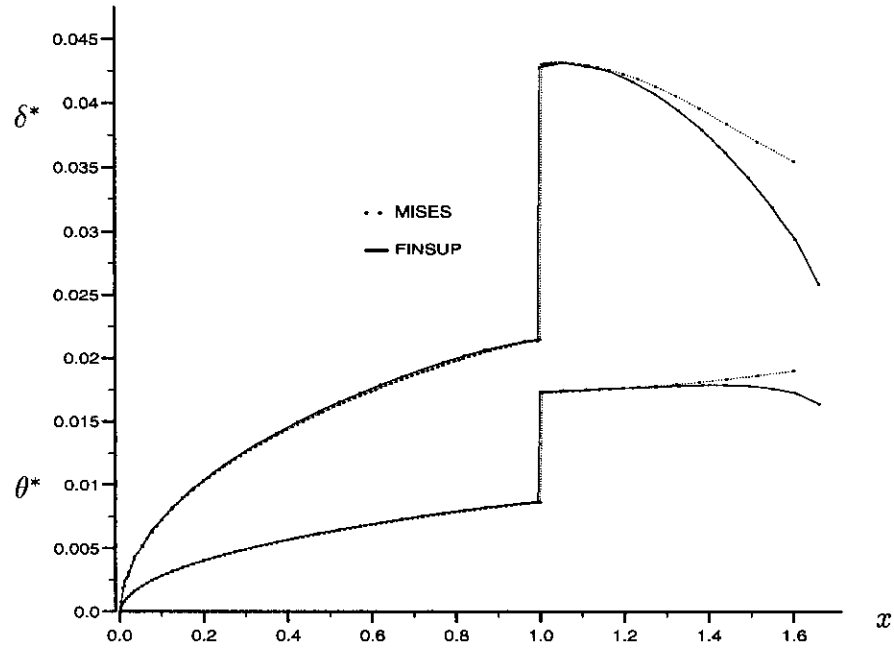

FIG. 8. The displacement and the momentum thickness.

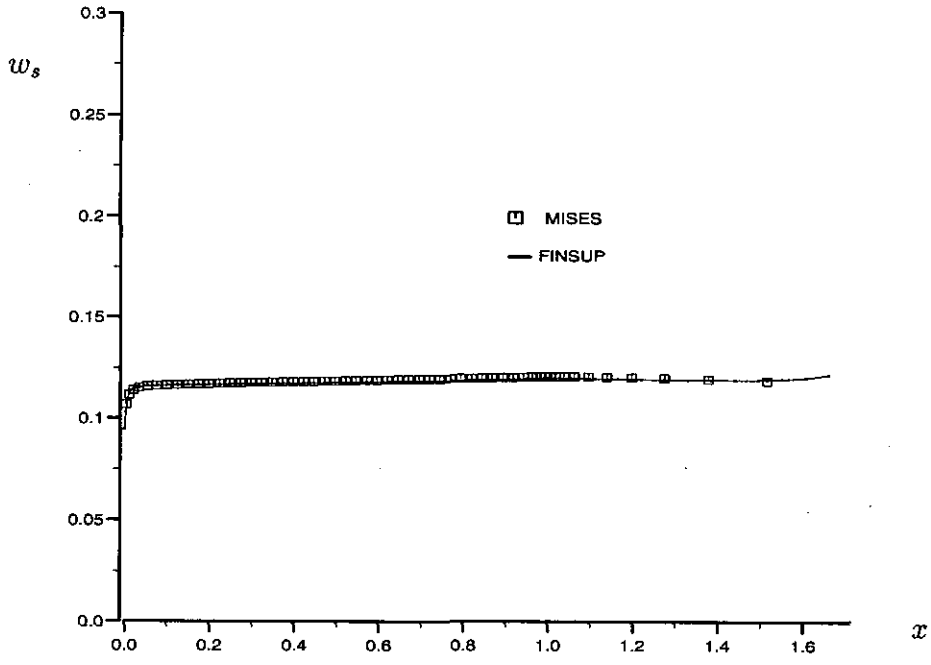

FIG. 9. The velocity distribution.

the grid points. The inviscid problem takes three iterations to converge while the overall algorithm converges in eight iterations. The displacement and the momentum thickness are shown in Figs. 11 and 12 and the pressure distribution is shown in Fig. 13. Free transition is used here and laminar separation bubbles are formed on both the pressure and suction sides at $x = 0.2$ and $x = 0.45$, respectively. In both sides, the transition points have been predicted at the end of the separation bubbles, quickly forcing reattachment, and thus setting the bubble length. The effect of this can be easily seen from the surface pressure distribution; the separation bubbles induce a slow variation in the pressure which is terminated by a strong adverse pressure gradient at reattachment. The results reported in [15] is reproduced here in Fig. 14 for comparison.

The third test case analyzes transonic flow over a compressor blade. The mesh is shown in Fig. 15. The Reynolds number is 1.436×10^6 and the transition point is forced at 0.5% of the total arc length of the blade on both the upper and the lower surface. The upwind formula (3.16) is used throughout except along the wake, where the average formula (3.15) is used in-

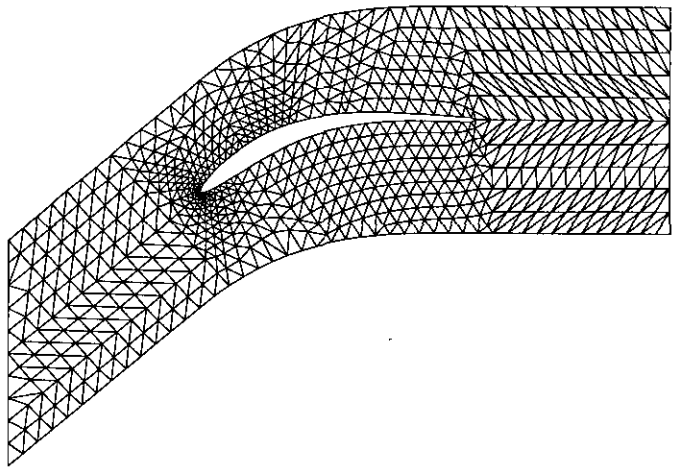

FIG. 10. The mesh for test case 2.

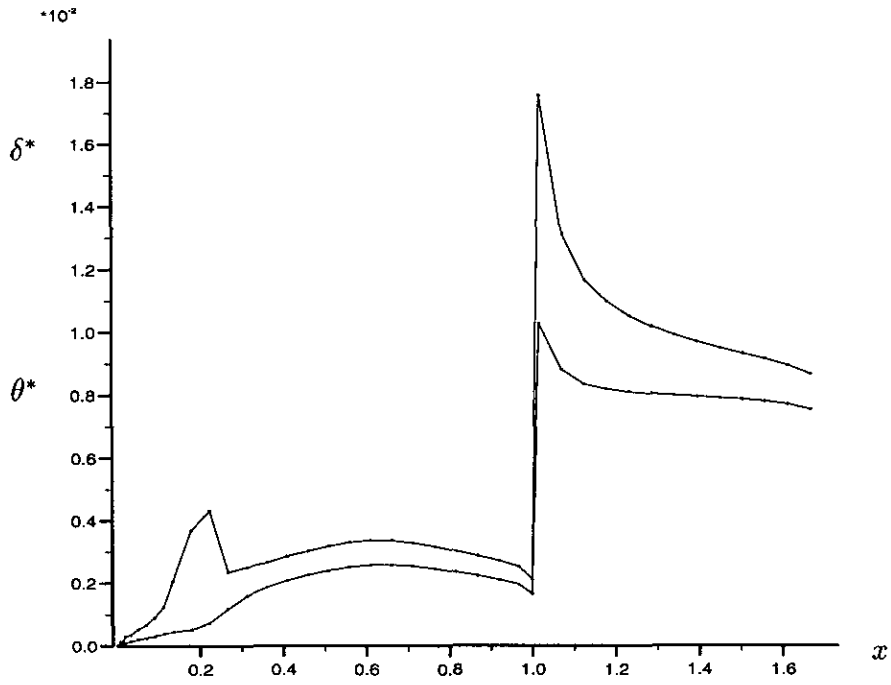

FIG. 11. The displacement and the momentum thickness on the pressure side.

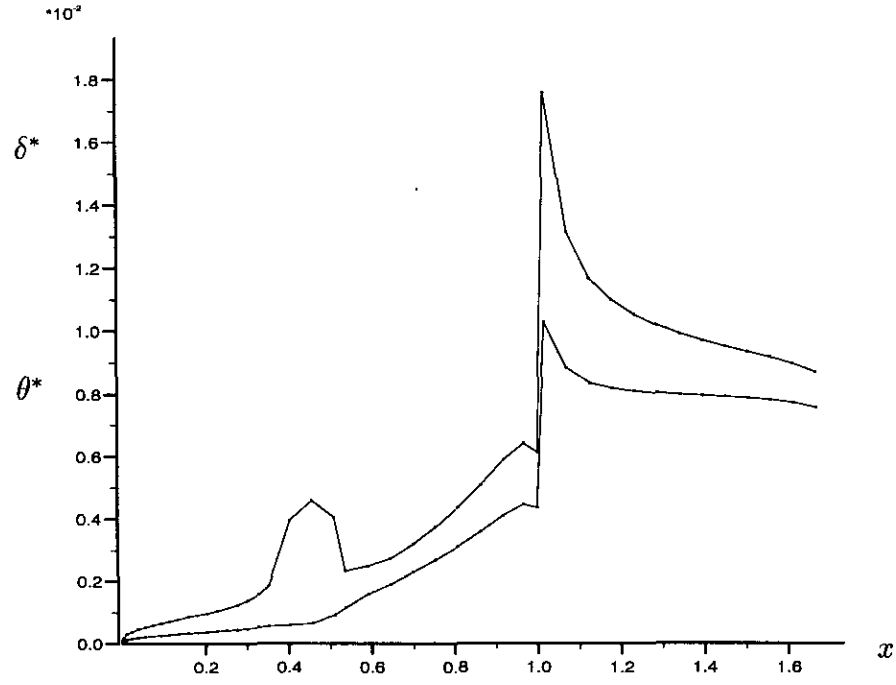

FIG. 12. The displacement and the momentum thickness on the suction side.

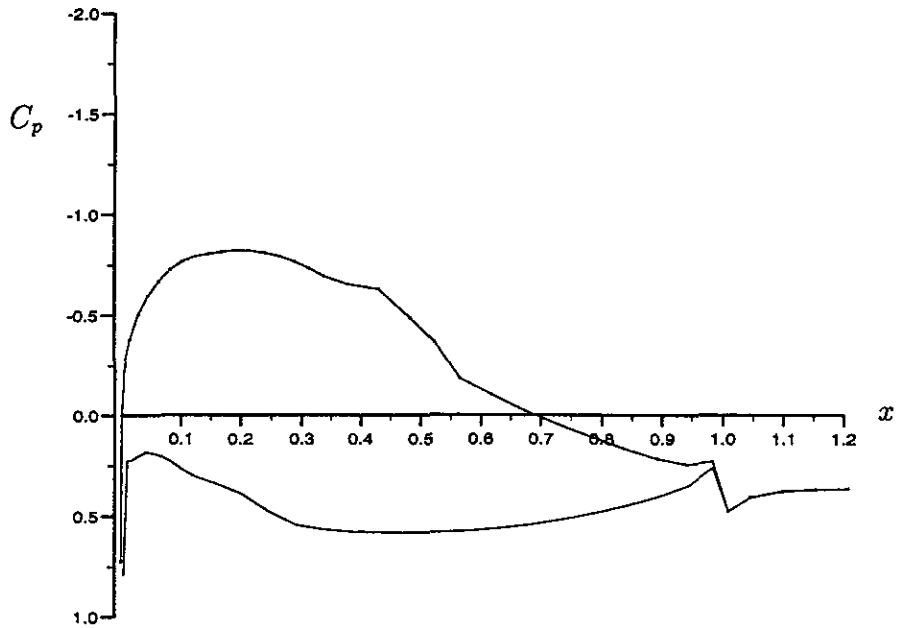

FIG. 13. The pressure distribution.

stead. For comparison purpose, the pressure coefficient C_{p_0} defined by

$$C_{p_0} = \frac{p_{0_{in}} - p}{p_{0_{in}} - p_{in}} \tag{4.2}$$

is calculated here, where p_{in} and $p_{0_{in}}$ denote the pressure and the total pressure at the inlet. When the inlet Mach number is 0.83, the inlet and the outlet angle of attack is 59° and 46°, respectively. The inviscid problem takes seven iterations to converge while the overall algorithm converges in two more iterations. The displacement and the momentum thickness are shown in Figs. 16 and 17 and the pressure distribution is given in Fig. 18. When the inlet Mach number is 1.025, the inlet and the outlet angle of attack is 58° and 46.6°, respectively. The inviscid problem takes about 20 iterations to converge while the overall algorithm converges in 10 more iterations. The displacement and the momentum thickness are shown in Figs.

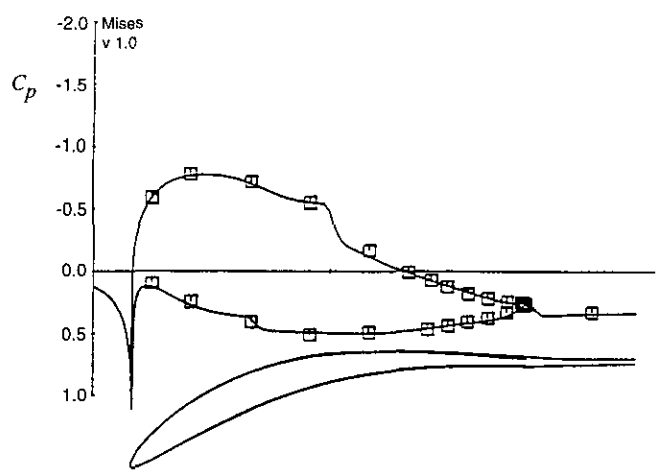

FIG. 14. The pressure distribution produced in [15].

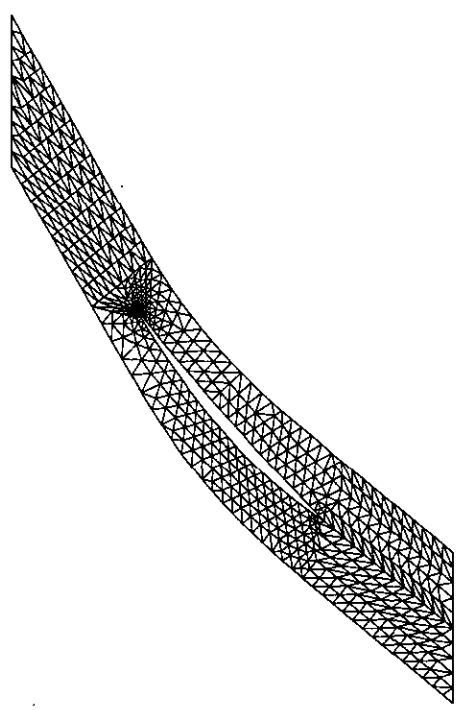

FIG. 15. The mesh for test case 3.

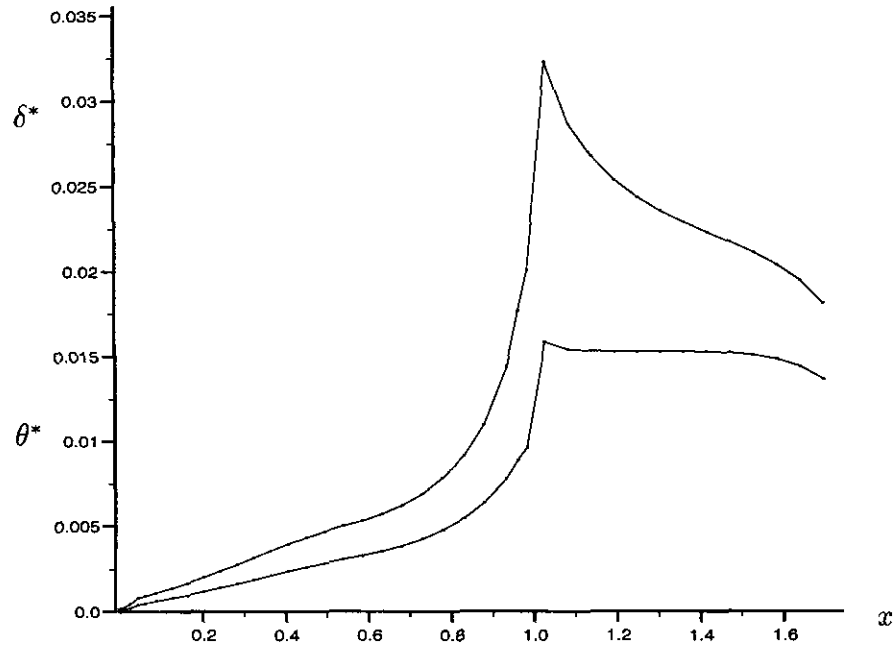

FIG. 16. The displacement and the momentum thickness on the suction side.

20 and 21 and the pressure distribution is given in Fig. 22. Note that there is a sudden increase in the displacement thickness at $x = 0.3$ on the suction side of the blade in Fig. 20. This is due to the present of a moderate-strength shock wave as can be seen in the pressure distribution. The results reported in [15] is reproduced here in Fig. 19 and Fig. 23 for comparison.

5. CONCLUDING REMARKS

The main aim of the paper has been to describe a new simultaneous coupling method to solve the viscous–inviscid coupling analysis problem. The coupling method is based on the use of the transpiration technique to simulate the effect of

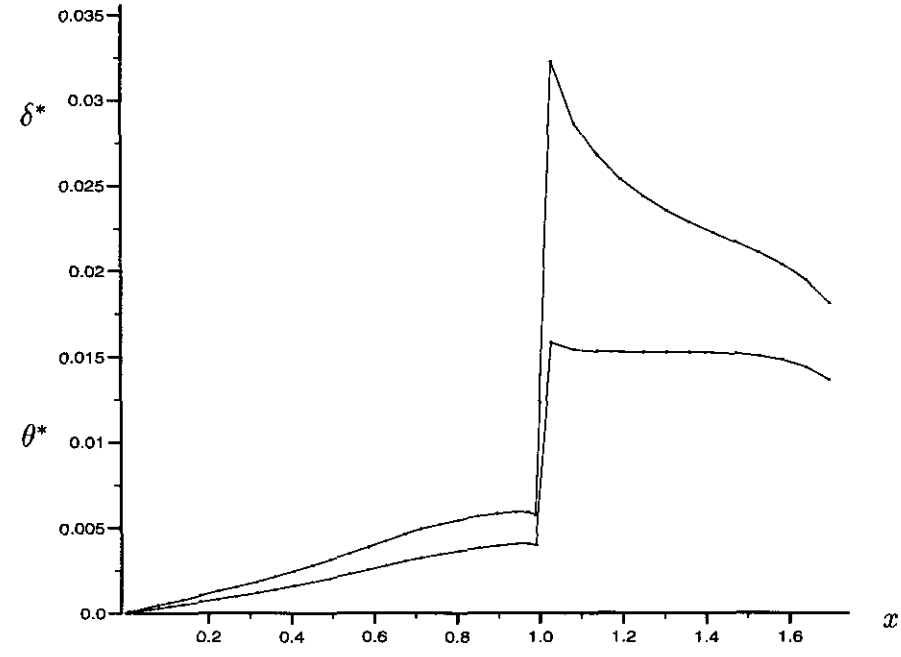

FIG. 17. The displacement and the momentum thickness on the pressure side.

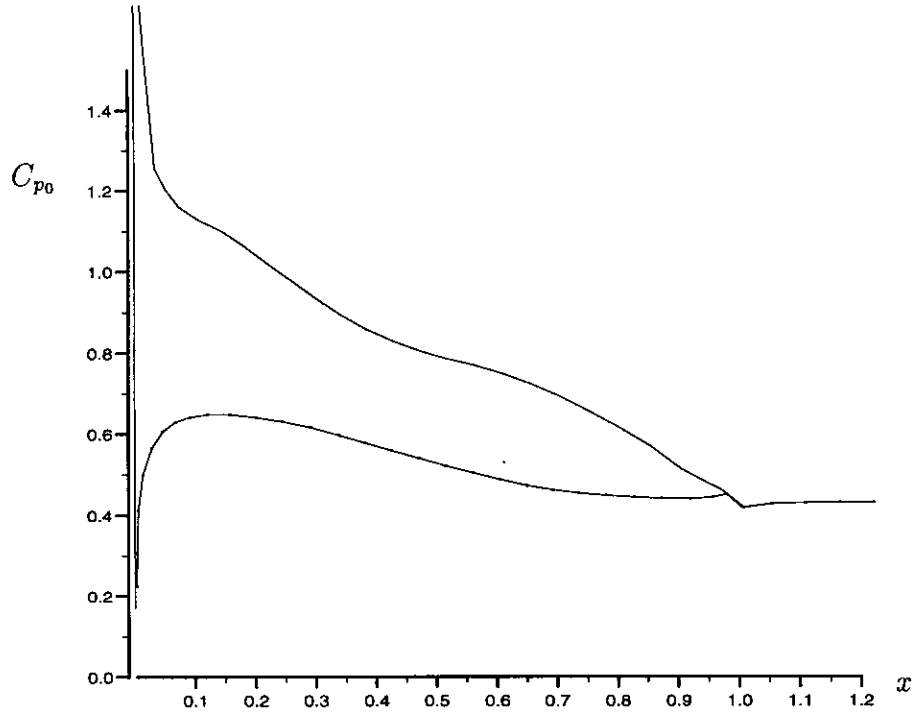

FIG. 18. The pressure distribution.

the displacement thickness. The applicability of the Newton–Raphson technique to solving the entire coupled nonlinear system of equations has been demonstrated. The numerical results have shown that the method can handle fairly thick boundary layer developments, separation bubbles, and shock-induced separation; and the convergence rate of the method is very satisfactory.

In the method, the effect of streamline radius and streamtube height variations have been ignored. It would be of interest to include these effects into the method to further improve the accuracy. Also, since the simple transpiration model (2.14) has been used, the exact location of the surface streamline along the wake is not determined. Although it is not a problem with great practical interest, still it is certainly of interest to know whether the use of more accurate transpiration models will enable such a task.

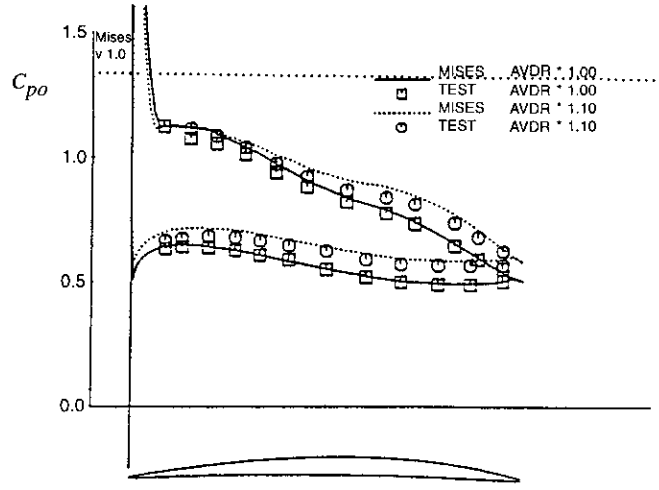

FIG. 19. The pressure distribution produced in [15].

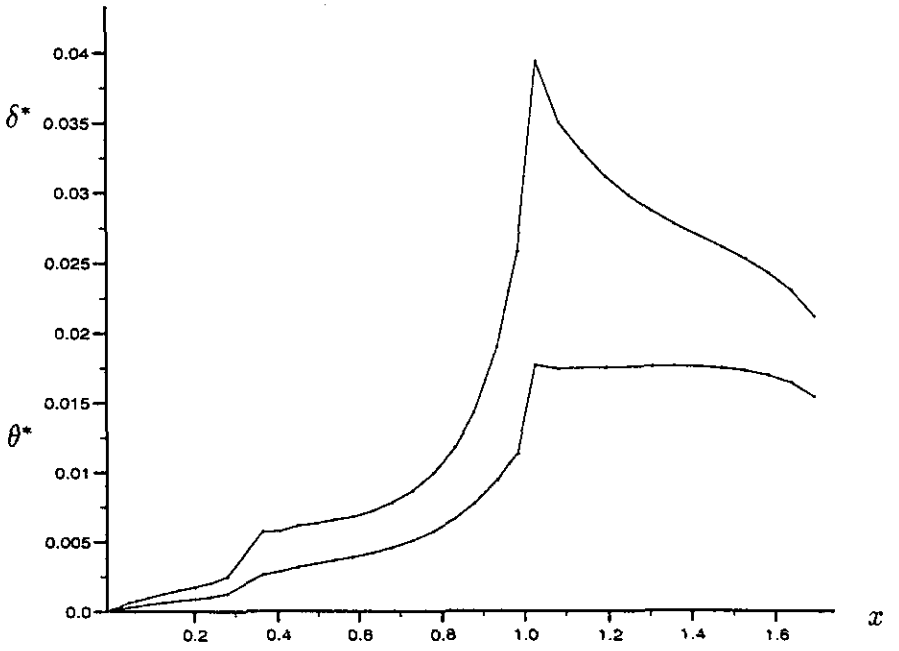

FIG. 20. The displacement and the momentum thickness on the suction side.

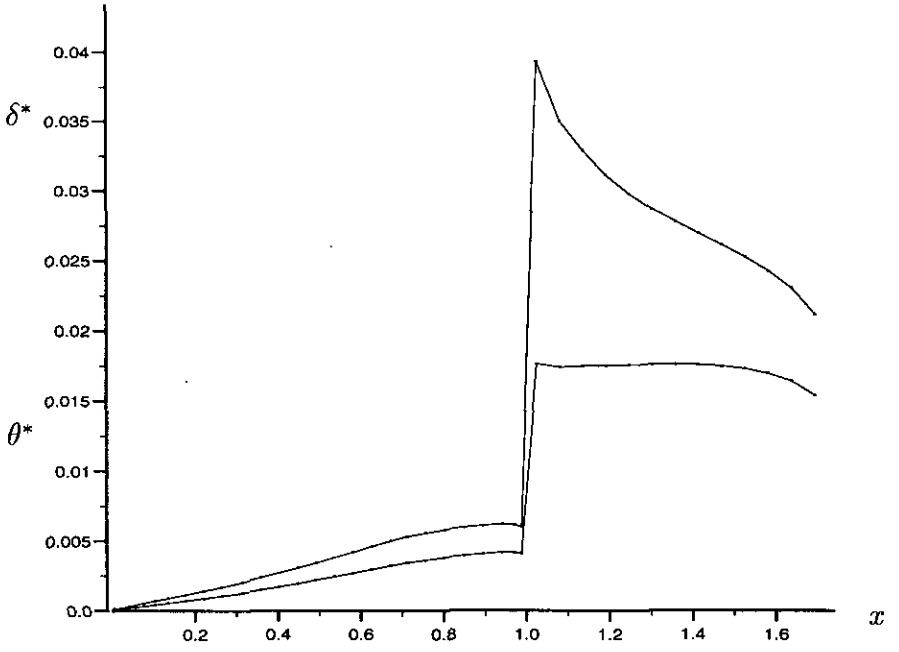

FIG. 21. The displacement and the momentum thickness on the pressure side.

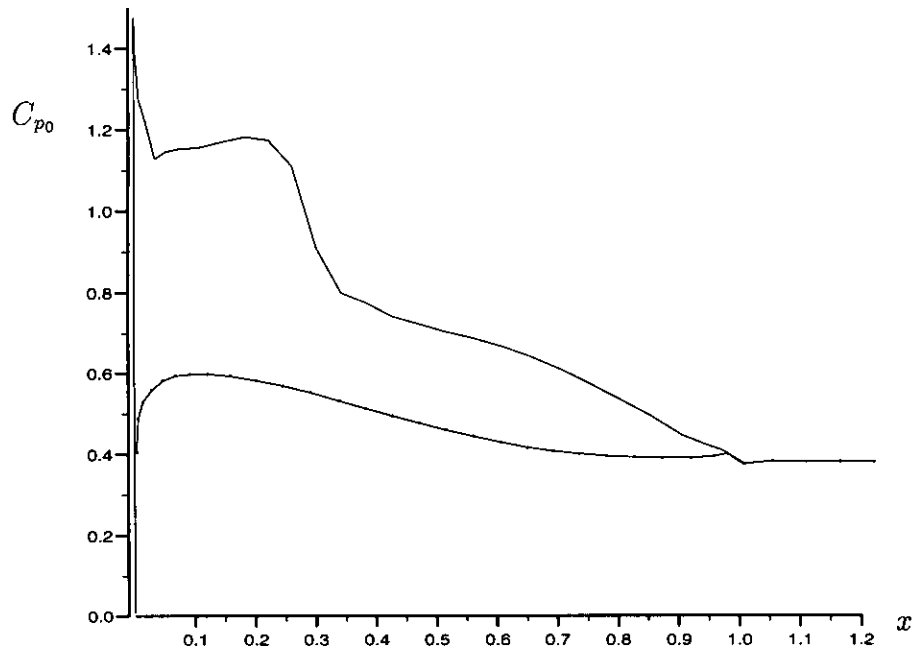

FIG. 22. The pressure distribution.

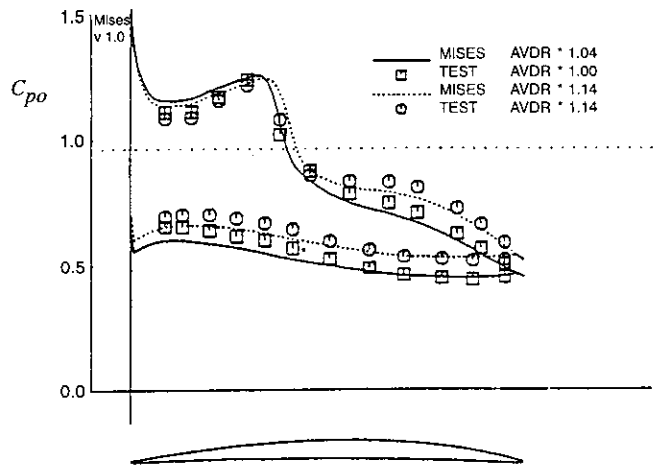

FIG. 23. The pressure distribution produced in [15].

ACKNOWLEDGMENTS

This research was supported by Rolls-Royce plc. The authors thank Rolls-Royce plc for providing the FINSUP package and Professor M. Drela at MIT for providing the MISES package.

REFERENCES

1. J. D. Anderson, *Fundamentals of Aerodynamics* (McGraw–Hill, New York, 1984).
2. H. Deconinck and C. Hirsch, ASME Paper, 83-GT-135, 1983 (unpublished).
3. M. Drela, Ph.D. thesis, MIT, 1985 (unpublished).
4. M. Drela and M. B. Giles, *AAIA J.* **25**(10), 1347 (1987).
5. M. Hafez, J. South, and E. Murman, *AAIA J.* **17**(8), 838 (1979).
6. C. Hirsch, *Numerical Computation of Internal and External Flows,* Vol. 1 (Wiley, New York, 1988).
7. Y. K. Ho, Theoretical Science Group Report 0425, Rolls-Royce plc, Derby, 1989 (unpublished).
8. T. L. Holst and W. F. Ballhaus, *AAIA J.* **17**(2) 1038 (1979).
9. C. J. Hwang, F. L. Jiang, J. M. Hsieh, and S. B. Chang, *Trans. ASME* **110,** 532 (1988).
10. H. L. Moses, R. R. Jones, and W. F. O'Brien, *AAIA J.* **16**(1), 61 (1978).
11. P. Stow and S. P. Newman, Theoretical Science Group Report 0343, Rolls-Royce plc, Derby, 1987 (unpublished).
12. A. E. P. Veldman, *AAIA J.* **19**(1), 79 (1981).
13. A. E. P. Veldman, "A Numerical View on Strong Viscous–Inviscid Interaction," in *Computational Methods in Viscous Flows, Recent Advances in Numerical Method in Fluids,* Vol. 3, edited by W. G. Habashi (Pineridge Press, Swansea, 1984).
14. D. S. Whitehead and S. G. Newton, *Int. J. Numer. Methods Fluids* **5,** 115 (1985).
15. H. H. Youngren, M. Sc. thesis, MIT, 1990 (unpublished).